## PAPER

# Low temperature fabrication of $Fe_2O_3$ nanorod film coated with ultra-thin $g$-$C_3N_4$ for a direct z-scheme exerting photocatalytic activities†

Suhee Kang, [ID] [a] Joonyoung Jang,[a] Rajendra C. Pawar, [ID] [b] Sung-Hoon Ahn [ID] [c] and Caroline Sunyong Lee [ID] *[a]

We engineered high aspect ratio $Fe_2O_3$ nanorods (with an aspect ratio of 17 : 1) coated with $g$-$C_3N_4$ using a sequential solvothermal method at very low temperature followed by a thermal evaporation method. Here, the high aspect ratio $Fe_2O_3$ nanorods were directly grown onto the FTO substrate under relatively low pressure conditions. The $g$-$C_3N_4$ was coated onto a uniform $Fe_2O_3$ nanorod film as the heterostructure, exhibiting rational band conduction and a valence band that engaged in surface photoredox reactions by a direct z-scheme mechanism. The heterostructures, particularly 0.75g-$C_3N_4$@$Fe_2O_3$ nanorods, exhibited outstanding photocatalytic activities compared to those of bare $Fe_2O_3$ nanorods. In terms of 4-nitrophenol degradation, 0.75g-$C_3N_4$@$Fe_2O_3$ nanorods degraded all of the organic pollutant within 6 h under visible irradiation at a kinetic constant of $12.71 \times 10^{-3}$ $min^{-1}$, about 15-fold more rapidly than bare $Fe_2O_3$. Further, the hydrogen evolution rate was 37.06 $\mu$mol $h^{-1}$ $g^{-1}$, 39-fold higher than that of bare $Fe_2O_3$. We suggest that electron and hole pairs are efficiently separated in $g$-$C_3N_4$@$Fe_2O_3$ nanorods, thus accelerating surface photoreaction *via* a direct z-scheme under visible illumination.

## 1. Introduction

Efforts to replace traditional fossil fuels are increasing because of the energy crisis and environmental contamination.[1,2] One of the many fascinating green technologies is photocatalytic degradation of organic pollutants and sustainable hydrogen production employing solar energy.[3–5] Many inorganic,[6] organic,[7] metal,[8] metal oxide,[9–13] and non-metal[14] materials have been used to reduce wastewater pollution and generate sustainable energy. However, the rapid recombination rates of charge carriers on catalytic surfaces reduce the photocatalytic efficiencies of single-component catalysts. Thus, semiconductor-based photocatalysts have received considerable attention; heterostructures of many materials afford reasonable band levels, maximizing rapid photocatalysis.[15–18] As the conduction and valence band levels differ, electron/hole pairs created using solar energy do not readily combine, improving photocatalytic performance. Nevertheless, heterostructure photo-oxidation/reduction reactions are compromised by the short energy bands of heterostructures compared to single-phase materials.[19]

The direct z-scheme, which recombines weaker oxidative holes and reductive electrons from semiconductors, has emerged as a major research area because the scheme may improve surface charge transfer and separation.[20–22] Various direct z-scheme photocatalysts have been studied, including g-$C_3N_4$/$Ag_3PO_4$,[23] $Fe_2O_3$/$Cu_2O$,[24] and $Bi_2O_3$/g-$C_3N_4$.[25] However, these heterostructures lack stability when exposed to sunlight and are difficult to synthesize. Useful heterostructures would be simply synthesized and exhibit excellent stability.

Recently, graphitic carbon nitride (g-$C_3N_4$), a polymeric non-metallic semiconductor, has been widely studied as a photocatalyst. Fabrication is inexpensive and simple, the material is carbon/nitrogen-rich and is non-toxic.[26] Furthermore, g-$C_3N_4$ exhibits a band gap of 2.6 eV, which is eminently suitable in terms of pollutant degradation and hydrogen evolution.[27–29] However, pure g-$C_3N_4$ exhibits rapid recombination of photogenerated electron/hole pairs, severely compromising photocatalytic activity. To reduce the recombination rate, heterostructures using different conduction and valence bands to host (reducing) electrons and (oxidizing) holes are required.[30–34]

The transition metal oxide $Fe_2O_3$ can utilize solar light of wavelengths up to 600 nm; the band gap is ~2.1 eV. Thus, $Fe_2O_3$ exhibits great potential because of its low cost, abundance, and good chemical stability.[35] Moreover, $Fe_2O_3$ has a 2.38 eV valence

[a]*Department of Materials and Chemical Engineering, Hanyang University, Ansan, Gyeonggi-do, 15588, South Korea. E-mail: sunyonglee@hanyang.ac.kr*

[b]*Department of Energy Engineering, Hanyang University, Seoul, 04763, South Korea*

[c]*Department of Mechanical and Aerospace Engineering, Seoul National University, Seoul, 08826, South Korea*

† Electronic supplementary information (ESI) available. See DOI: 10.1039/c8ra04499f
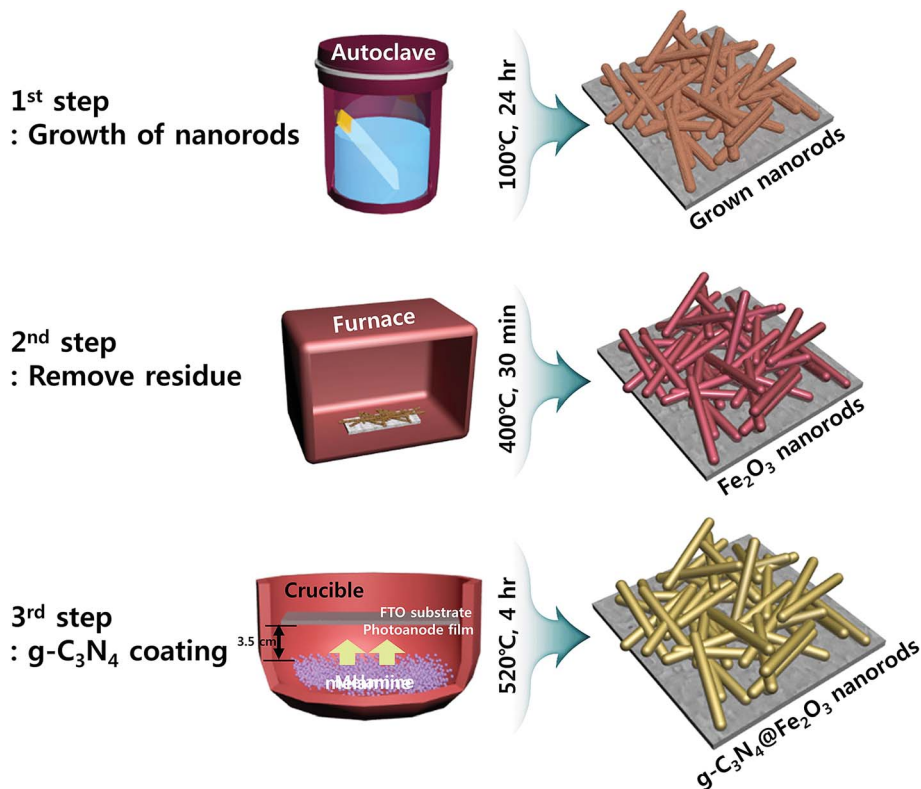
**Scheme 1** Fabrication of facile and simple heterostructures of g-$C_3N_4$@$Fe_2O_3$.

band that can be exploited by the direct z-scheme mechanism of photocatalysis; thus, $Fe_2O_3$ can serve as a photoactive material.[36] However, $Fe_2O_3$ has a short hole diffusion length and exhibits rapid charge recombination, rendering the photocatalytic efficiency low.[37] Therefore, $Fe_2O_3$ must be combined with other semiconductors in heterostructures featuring separation of electron/hole pairs, allowing photo-oxidation and reduction using the direct z-scheme system.

Many $Fe_2O_3$/g-$C_3N_4$ heterostructures, including powder-like bulk composites, have been developed to eliminate organic pollutants and evolve $H_2$ under visible irradiation.[38–41] However, such heterostructures, when exposed to solar illumination, exhibit gradual reductions in electron movement, compromising photocatalysis compared to that of one-dimensional (1D) structures.[42] To overcome this problem, we fabricated g-$C_3N_4$@1D $Fe_2O_3$ nanorods using the simplest procedure; *In situ* growing of high aspect ratio of $Fe_2O_3$ nanorods with solvothermal method at 100 °C for 24 hours was followed by ultra-thin coating of g-$C_3N_4$ layer using melamine precursors with thermal evaporation method to degrade 4-nitrophenol (4-NP) and evolve $H_2$. The prepared 1D $Fe_2O_3$ nanorods coated with ultra-thin g-$C_3N_4$ layers can be fabricated in a straightforward, cost-effective manner to show the direct z-scheme system. We explored the physicochemical properties of our materials and optimized the g-$C_3N_4$@$Fe_2O_3$ nanorods in terms of photocatalysis; we then compared the materials to that of bare $Fe_2O_3$ nanorods for its potential application in photocatalytic fields such as $H_2$ evolution, artificial photosynthesis or even more electrocatalysts and battery applications.

## 2. Experimental

### 2.1 Materials

We used the $Fe_2O_3$ precursor ferric chloride ($FeCl_3$) and the g-$C_3N_4$ precursor melamine (Junsei, Japan). Sodium nitride ($NaNO_3$), hydrochloric acid (HCl), acetonitrile, sodium sulfate ($Na_2SO_4$) and hydrogen peroxide ($H_2O_2$) were all purchased from Daejung (Korea). Triethanolamine (TEOA) (Samchun, Korea) and $H_2PtCl_2$ (Sigma-Aldrich, USA) were used to trigger $H_2$ evolution. Conductive fluorine-doped tin oxide (FTO, 15 mΩ) served as the photoanode film. *p*-nitrophenol was purchased from Kanto (Japan). All chemicals were used without further purification.

### 2.2 Preparation of a $Fe_2O_3$ photoanode and g-$C_3N_4$ coating

$Fe_2O_3$ photoanodes were prepared on FTO substrates using a solvothermal method under relatively low pressurized condition.[43] Conventionally, pressurized condition is mostly used for fabrication of $Fe_2O_3$ photoanodes. However, we have developed relatively low pressure process to fabricate high aspect ratio of nanorods (almost 17 : 1) film with extreme uniformity onto FTO substrate through *in situ* process. Prior to $Fe_2O_3$ growth, the substrates were sequentially cleaned with acetone, ethanol, and distilled water with sonication for 5 min each time and dried in an oven. 0.2 M $FeCl_3$ was dissolved in 35 mL of distilled water while 1.4 M $NaNO_3$ and 0.5 mL of HCl were added. After complete dissolution, 15 mL of acetonitrile was added and this mixture was stirred for 30 min. Plasma-enhanced chemical vapor deposition (PECVD) was used to perform $O_2$ plasma
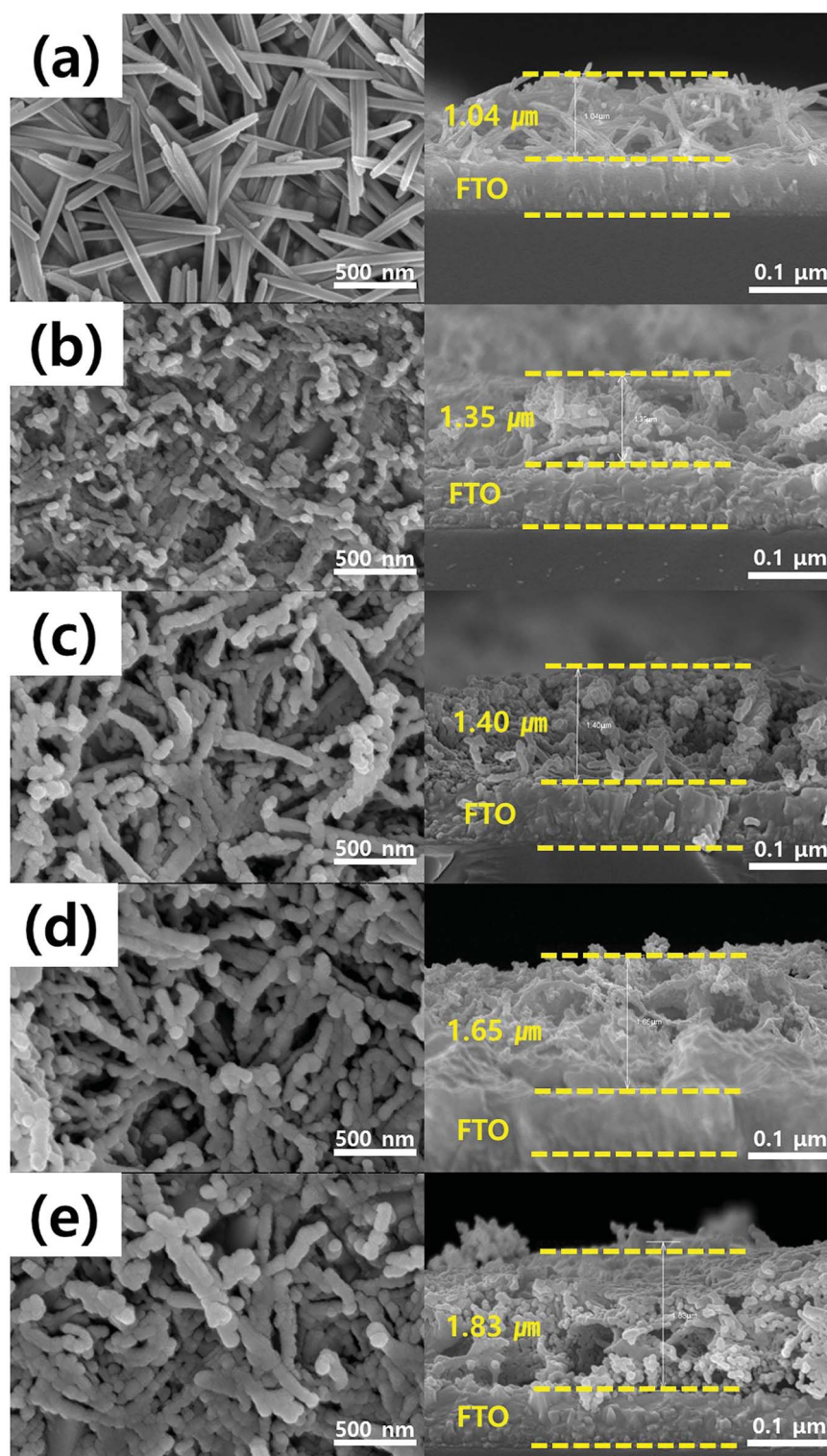
**Fig. 1** SEM micrographs of (a) bare $Fe_2O_3$, (b) 0.25g-$C_3N_4$@$Fe_2O_3$, (c) 0.5g-$C_3N_4$@$Fe_2O_3$, (d) 0.75g-$C_3N_4$@$Fe_2O_3$, and (e) 1g-$C_3N_4$@$Fe_2O_3$; cross-sections (right-hand) and surface views (left-hand).

treatment, removing any pollutants. The solution described above was transferred to 100 mL of Teflon-lined molds and held at 100 °C for 24 h in a box furnace. Afterwards, the film was taken out from the mold and dried at ambient atmosphere. Then, the dried film was annealed at 400 °C for 30 min and

washed several times with distilled water in order to remove any residues left on the top of the film. Fig. S1(b)† shows no transformation of this material to hematite phase after annealing at 400 °C since no peak for hematite is detected. In order to make successful transformation to hematite $Fe_2O_3$
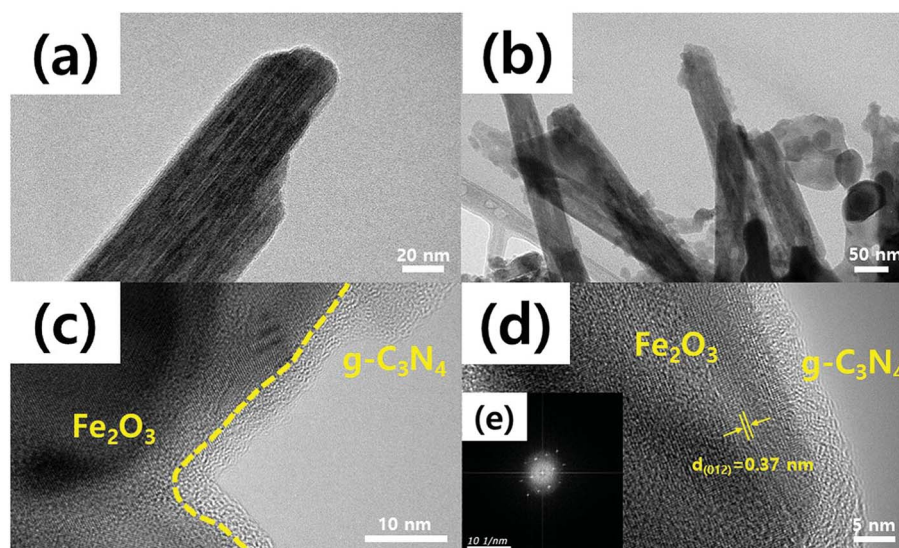
**Fig. 2** Transmission electron microscopy (TEM) images of (a) bare $Fe_2O_3$ nanorods and (b) 0.75g-$C_3N_4$@$Fe_2O_3$. (c) High-magnification image of the g-$C_3N_4$ coating layer on $Fe_2O_3$ nanorods. (d) The lattice distance of $Fe_2O_3$ and (e) the fats Fourier transform (FFT) [inset in (d)].

phase, this washed film was annealed again at 520 °C for 4 h where this is denoted as "bare $Fe_2O_3$" for clarification. To coat the photoanodes with a g-$C_3N_4$ layer to form heterostructure, various amounts of melamine (0.25, 0.5, 0.75, and 1 g) in powder form were used in alumina crucible for optimization of heterostructure. Photoanode film was placed 3.5 cm apart from the melamine powders, facing each other in the crucible as shown in Scheme 1. Then, the melamine powders were sintered and coated on the surface of the photoanode film through thermal evaporation method at 520 °C for 4 h (10 °C min$^{-1}$). Finally, g-$C_3N_4$-coated photoanode films were successfully obtained by this evaporation of melamine powders as the overall procedure is represented in Scheme 1.

### 2.3 Evaluation of photocatalytic activity

Photocatalytic activity was evaluated using 0.02 mM 4-NP in distilled water. The g-$C_3N_4$@$Fe_2O_3$ photoanode films were placed in 250 mL amounts of this solution and 0.5 mL of $H_2O_2$ was added prior to illumination to accelerate catalytic activity, followed by stirring for 30 min in the dark. The $H_2O_2$ is used to produce hydroxyl radical (·OH) and OH$^-$ species, reducing $Fe^{3+}$ to $Fe^{2+}$ under light condition.[51] Then, 300W Xe arc lamp (>400 nm cut-off filter) was used to illuminate the solution while amount of 3 mL was collected every 1 h until the degradation was complete.

### 2.4 Photoelectrochemical performance

Photoelectrochemical (PEC) performance was evaluated using a three-electrode in quartz cell. Graphite and Ag/AgCl served as the counter-electrode and reference electrode, respectively. The electrolyte solution was 0.5 M $Na_2SO_4$ and PEC performance was analyzed using a Xe arc lamp (300 W, model 66984; Oriel, USA) with cut-off filter (>400 nm). A transient photocurrent was applied at 1 V of bias potential *versus* the Ag/AgCl reference

electrode, with light-chopping every minute to allow the response to be observed. Stability testing was performed for 40 h under the same conditions. Linear sweep voltammetry (LSV) was performed at a 20 mV s$^{-1}$ scan rate from −1 to 1 V. Electrochemical impedance spectroscopy (EIS) was performed from $10^5$ to 0.01 Hz at an amplitude of 20 mV under both dark and light conditions.

### 2.5 Photocatalytic $H_2$ production

Photocatalytic $H_2$ evolution was assessed with the aid of a 250 mL quartz reactor in a closed-gas system under visible illumination. The light source was a 300 W Xe arc lamp fitted with an ultraviolet (UV) cut-off filter (>400 nm), thus delivering only visible light. 10 mg of as-prepared catalytic powder were dispersed in135 mL of distilled water until they are completely mixed. Then, 9 vol% of TEOA was added into that of aqueous solution to be acted as hole capture. A 1 wt% Pt solution served as the co-catalyst *via in situ* photodeposition. The solutions were uniformly dispersed prior to reaction. The suspension was then transferred to the quartz reactor and purged with $N_2$ gas to remove $O_2$. The reactor was sealed with a septum and purged with Ar gas to completely eliminate all air. Evolved gas was detected by a pulsed discharge detector fitted to a gas chromatograph (model 6500GC; YL Instruments, Korea); helium served as the carrier gas.

### 2.6 Characterization

g-$C_3N_4$ and $Fe_2O_3$ morphologies were studied using a scanning electron microscope (SEM; model S4800; Hitachi, Japan) and a transmission electron microscope (TEM) (model JEM 2100F; JEOL, Japan). The crystalline structure and other properties of the $Fe_2O_3$ phase were analyzed by X-ray diffraction (XRD) (D/Max-2500/PC instrument; Rigaku, USA; Cu-Kα source), Fourier-transform infrared spectroscopy (FTIR) (iS10

instrument; Thermo Fisher Scientific, UK), and X-ray photo-electron spectroscopy (XPS) (Sigma Probe instrument, Thermo Fisher Scientific; Al Kα source); these modality es were also used to confirm the presence of g-$C_3N_4$ coatings. The band gap energy was calculated *via* UV-visible spectroscopy (UV-Vis) (model V650; JASCO, Japan). Photoluminescence (PL) (SC-100 instrument; Dongwoo, Korea) and Raman spectroscopy (S-Ram instrument; Dongwoo) were employed to monitor the recombination rate of $Fe_2O_3$ and g-$C_3N_4$ under light excitation at 325 nm. All PEC analyses were performed using a potentiostat (Versastat 4 instrument; Princeton Applied Research, USA). The absorbances of photocatalytically degraded solutions were measured *via* UV-Vis spectroscopy.

## 3.   Results and discussion

### 3.1   Morphology

We fabricated heterostructures using sequential solvothermal and thermal evaporation methods. We obtained top and cross-sectional views to explore how morphologies varied by the extent of coating. Prior to structural observations, chemically grown photoanode films were annealed first at 400 °C for 30 min and then washed several times with distilled water to remove any residue within nanorods that might interfere with electron transfer. As a result, the microstructure showed that the residue was perfectly removed while these nanorods are still strongly attached to the FTO substrate even after washing (Fig. S1(a)†). However, the annealing process at 400 °C for 30 min followed by washing treatments did not convert its structural phase into hematite phase since high intensity of $NaNO_3$ peaks (JCPDS no. 36-1474) and $SnO_2$ peaks (JCPDS no. 77-0451) were shown in Fig. S1(b).† To obtain pure hematite $Fe_2O_3$ nanorods, washed photoanode film was again annealed at 520 °C for 4 h. And finally, the bare $Fe_2O_3$ film was acquired.

As shown in Fig. 1(a), the FTO substrate contained only $Fe_2O_3$ nanorods, the surfaces of which were smooth. The observed high aspect ratio would be expected to improve electron transfer and photoactivity (Fig. S2†). After the g-$C_3N_4$ precursor was evaporated during optimum sintering at 520 °C, nano-sized, agglomerated g-$C_3N_4$ particles were clearly attached to the $Fe_2O_3$ nanorods. The thicknesses of these microstructures averaged around 1.5 μm (from the bottom of the $Fe_2O_3$ nanorod to the top of the g-$C_3N_4$ coating). The thickness of the heterostructured films increased as the amount of the melamine precursor increased, from 0.25 to 0.5, 0.75 and 1 g, resulting in increasing thermal evaporation of g-$C_3N_4$ [Fig. 1(b)–(e)]. A previous study indicated that the precursor level should be varied to optimize the coating layer; thicker layers obstruct incident light and reduce activity.[45] We performed energy-dispersive spectroscopy (EDS) mapping to reveal the elements of g-$C_3N_4$@$Fe_2O_3$ heterostructures; these were (as expected) iron, oxygen, carbon, and nitrogen (Fig. S3†). For comparison, the bulk g-$C_3N_4$ was observed for its microstructures in terms of agglomeration, reducing the active site from surface area as well as blocking electron pathway under illumination as shown in Fig. S4.† We thus confirmed that well-formed g-$C_3N_4$@$Fe_2O_3$
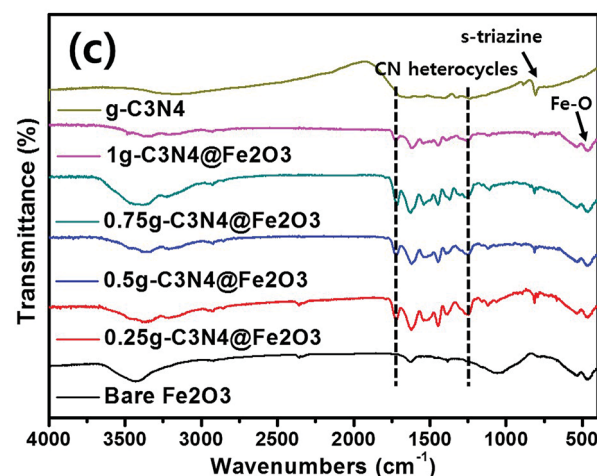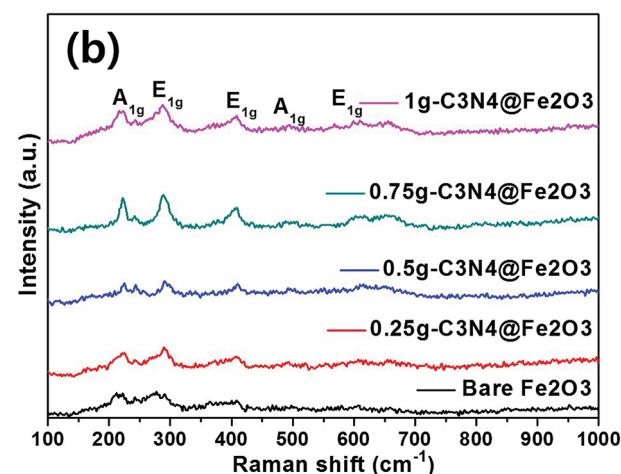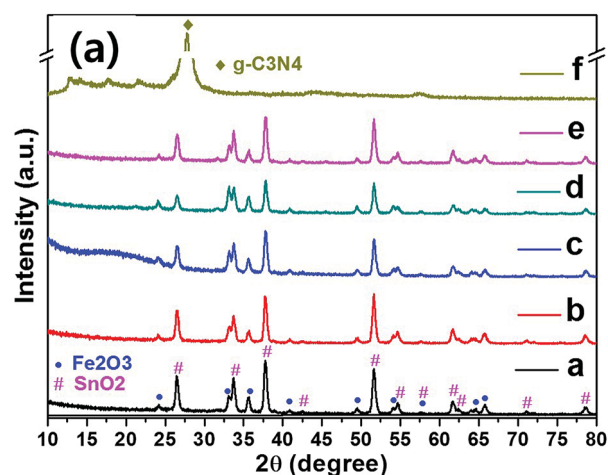


Fig. 3  (a) X-ray diffraction (XRD), (b) Fourier-transform infrared spectroscopy (FT-IR) and (c) Raman spectroscopy data for bare $Fe_2O_3$, 0.25g-$C_3N_4$@$Fe_2O_3$, 0.5g-$C_3N_4$@$Fe_2O_3$, 0.75g-$C_3N_4$@$Fe_2O_3$, 1g-$C_3N_4$@$Fe_2O_3$ and bulk g-$C_3N_4$.

heterostructures had been created *via* a simple chemical process.

The TEM was used to derive the precise dimensions of the $Fe_2O_3$ nanorods, the lattice distance, and the g-$C_3N_4$ thicknesses. Bare $Fe_2O_3$ nanorods were ~60 nm in diameter

[Fig. 2(a)]. All $Fe_2O_3$ nanorods had a high aspect ratio (16.7 : 1), enhancing the surface area and thus active sites. The TEM images of g-$C_3N_4$ coated onto $Fe_2O_3$ [Fig. 2(b) to (d)] showed that the $Fe_2O_3$ nanorods were fully covered with g-$C_3N_4$. Furthermore, the g-$C_3N_4$ coat was <10 nm in thickness, but this varied slightly because of yield effects during thermal evaporation. If g-$C_3N_4$ precursors are loaded onto $Fe_2O_3$ films to different extents under atmospheric conditions, g-$C_3N_4$ production levels will vary, affecting the final coating layers. Fast Fourier Transform (FFT) [Fig. 2(e)] revealed that the interplanar spacing in $Fe_2O_3$ was 0.37 nm, corresponding to the lattice distance of the (012) plane for $Fe_2O_3$. Thus, our heterostructures of 1D $Fe_2O_3$ nanorods covered with g-$C_3N_4$ sheets, were successfully synthesized using the relatively low pressurized solvothermal method which have shown good catalytic performance due to efficient separation of charge carriers right at the interface between g-$C_3N_4$ and $Fe_2O_3$, resulting in enhanced electron movements along with 1D structures.

## 3.2 Characterization

Fig. 3(a) shows the $Fe_2O_3$ crystallinities of bare $Fe_2O_3$ and all of the prepared heterostructures using XRD analysis. Distinct $Fe_2O_3$ peaks are evident at 24.10, 33.08, 35.61 and 51.58°, corresponding to the (012), (104), (110), and (116) planes, respectively. The structure was hematite in nature ($\alpha$-$Fe_2O_3$), as indicated by the JCPDS 01-084-0306 criteria, and the $Fe_2O_3$ lattice constants were $a = b = 4.69$ Å and $c = 13.83$ Å in the hexagonal structure. In the heterostructures, the sharp diffraction peaks indicated high-level $Fe_2O_3$ crystallinity and no impurity peak was appeared. The photoanode films were subjected to XRD and the diffraction peaks of the $SnO_2$ phase were thus observed (JCPDS no. 01-070-6995). The peaks for bulk g-$C_3N_4$ were observed to be (100) and (002) planes at 13° and 27°, respectively as shown in Fig. S4(b).† The initial peak for (100) plane was presented as the in-plane structural packing of triazine and the other intense peak for (002) plane was presented as the inter-planar spacing from aromatic group of g-$C_3N_4$.[14] However, g-$C_3N_4$ was not detected by XRD; overall, the g-$C_3N_4$ loadings were relatively low in heterostructure films. Raman spectroscopy was used to identify characteristic $Fe_2O_3$ peaks [Fig. 3(b)]. Principal peaks were evident at 217, 290, 407, 493, and 603 $cm^{-1}$, corresponding to the $A_{1g}$, $E_{1g}$, $E_{1g}$, $A_{1g}$, and $E_{1g}$ modes, respectively.[46] For the case of bulk g-$C_3N_4$, the intense peaks were observed at 483.2, 708.6, 754.4, 976.9, 1235.9, 1313.9 and 1566.8 $cm^{-1}$, relating g-$C_3N_4$ groups as shown in Fig. S4(c).† Among the Raman peaks, the peaks for g-$C_3N_4$ structures were presented at 483.2, 754.4, 976.9 and 1313.9 $cm^{-1}$.[47] Moreover, the initial peak of 708.6 $cm^{-1}$ was presented to be the s-triazine ring for g-$C_3N_4$ group. The peaks at 1235.9 and 1566.8 $cm^{-1}$ are observed to be the disorder in graphite structure and stretching mode in C=N bonding structure, respectively.[48] However, again, g-$C_3N_4$ peaks were not detected because the g-$C_3N_4$ levels were low. Therefore, we used FT-IR to analyze the molecular compositions. In Fig. 3(c), the $Fe_2O_3$ peaks at 534 and 467 $cm^{-1}$ correspond to stretching vibrations of the Fe–O bonds of $FeO_6$ octahedral and $FeO_4$

tetrahedral sites, respectively.[49] The bulk g-$C_3N_4$ was compared for its specific g-$C_3N_4$ patterns with ones for the heterostructures. The principal g-$C_3N_4$ peaks range from 1700 to 1200 $cm^{-1}$, corresponding to stretching vibrations of tri-s-triazine in the heterocyclic rings. In detail, the bands at 1448, 1370 and 1250 $cm^{-1}$ correspond to aromatic C–N stretching vibrations.[50] Furthermore, the band at 816 $cm^{-1}$ corresponds to the s-triazine unit of the graphite-like $sp^2$ bonding state. It is clearly confirmed that all g-$C_3N_4$ related peaks are shown in the as-fabricated heterostructures as well as bulk g-$C_3N_4$. Moreover, broad peaks at 3500–3000 $cm^{-1}$ corresponded to N–H and O–H stretching vibrations caused by surface adsorption of $H_2O$.[51] Thus, we have confirmed the presence of g-$C_3N_4$ on $Fe_2O_3$.

To explore the relationship between the C and N elements and Fe, XPS was performed as shown in Fig. 4. The typical Fe 2p spectrum of bare $Fe_2O_3$ features two different peaks (Fe $2p_{1/2}$ and Fe $2p_{3/2}$) of binding energies 709.0 eV and 722.8 eV, respectively [Fig. 4(a)]. Between these peaks, a satellite $Fe^{3+}$ peak is apparent. In the O 1s spectrum, bare $Fe_2O_3$ exhibits principal peaks at 528.0 eV, 528.2 eV, 529.9 eV, and 531.5 eV, which are mainly attributable to Fe–O bonding, lattice oxygen, the hydroxyl group, and surface-absorbed $H_2O$, respectively [Fig. 4(b)].[44] Fig. 4(c) shows the 0.75g-$C_3N_4$@$Fe_2O_3$ Fe 2p spectrum (peaks at 708.9 eV for Fe $2p_{1/2}$ and 722.7 eV for Fe $2p_{3/2}$) of the g-$C_3N_4$ coating. Fig. 4(d) shows similarly broad principal peaks at 528.0 eV, 529.0 eV, 529.7 eV, and 531.0 eV.[52] As g-$C_3N_4$ coated $Fe_2O_3$, C 1s and N 1s spectra were detected. The C 1s spectrum exhibits binding energies at 286.5, 285.4, 284.3, and 282.7 eV, corresponding to $sp^2$-hybridized carbon in the tri-s-triazine rings C=O, C–O, C–C and C=C bonding, respectively [Fig. 4(e)].[53,54] In the N 1s spectrum [Fig. 4(f)], the binding energy peaks at 396.1, 397.7, and 399.6 eV correspond to $sp^2$-hybridized nitrogen (C–N=C), tertiary nitrogen [N–(C)$_3$], and –$NH_2$ bonding, respectively, and were unique to the g-$C_3N_4$ moieties.[41] Fig. 4(g) and (h) showed the C 1s and N 1s spectrums of bulk g-$C_3N_4$ for comparison, respectively. The bulk g-$C_3N_4$ shows three different peak positions at 288.5, 287.2 and 283.9 eV in C 1s spectrum. The peaks for 288.5 eV, 287.2 eV are for $sp^2$-hybridized bonding of N–C=N in aromatic and C–N bonds in carbon species of bulk g-$C_3N_4$, respectively. The peak for 283.9 eV is assigned to the carbon contamination during the samples preparation. In N 1s spectrum, the main peak of 397.7 eV is ascribed to C=N–C bonding while the peak of 398.5 eV is ascribed to N–(C)$_3$ bonded group. The weaker peaks of 400.2 and 403.6 eV are attributed to amino functional groups in aromatic rings of g-$C_3N_4$ and π-excitation which is positively charged localization in heterocycles, respectively.[60] When the 0.75 g of melamine is coated onto $Fe_2O_3$ film to convert into g-$C_3N_4$ layer, the amounts of coating layer are considerably lower than that of bulk g-$C_3N_4$. Thus, the carbon and nitrogen spectrums of 0.75g-$C_3N_4$@$Fe_2O_3$ showed relatively low intensity compared to that of bulk g-$C_3N_4$ even though it represented the carbon and nitrogen-related bonding as shown in Fig. 4(e) and (f). Therefore, that obvious peak shift for C=N–C and N–(C)$_3$ at 397.7 and 398.5 eV suggest the chemically formed heterojunctions between $Fe_2O_3$ and g-$C_3N_4$.
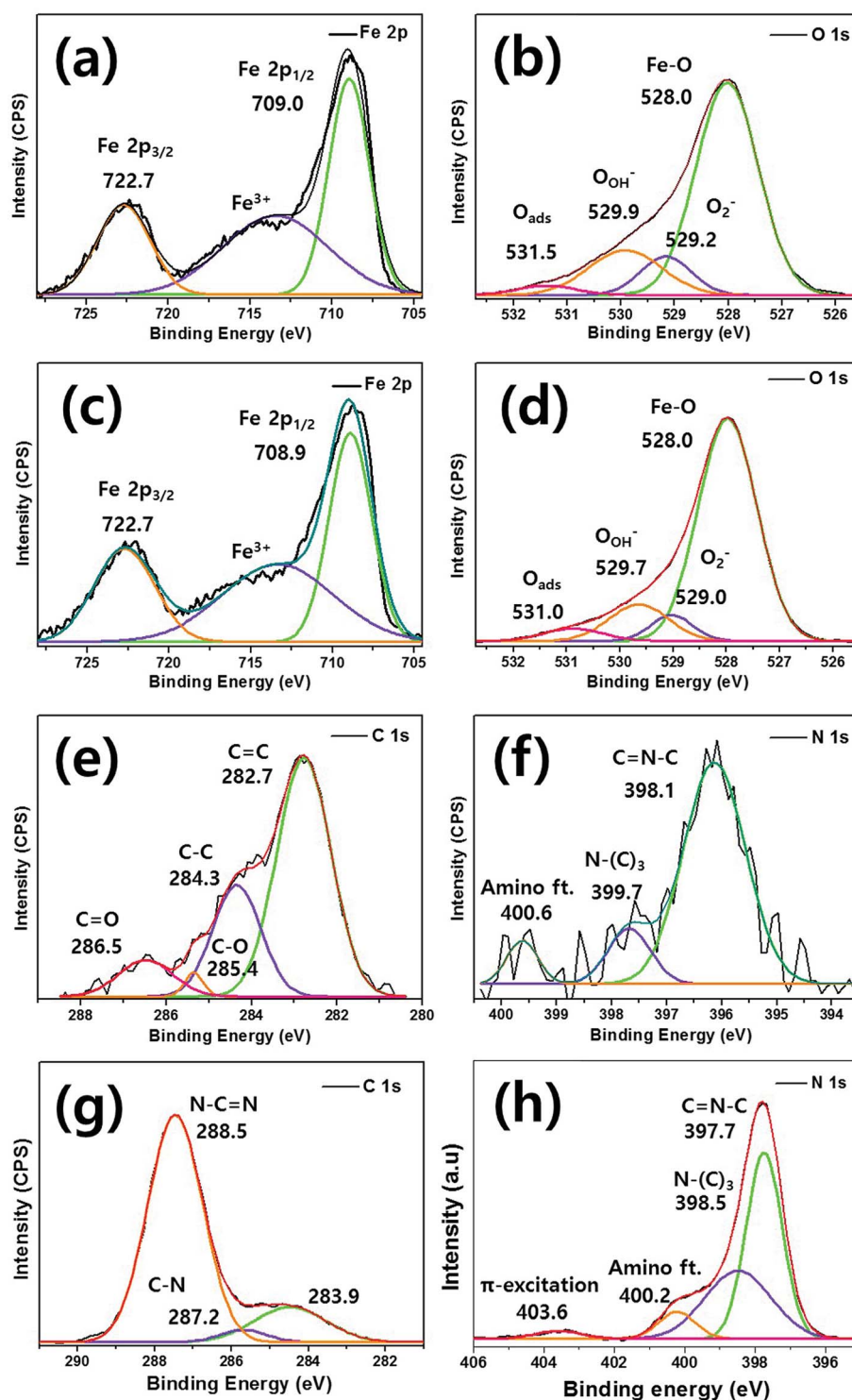
**Fig. 4** The chemical binding energies evident on bare $Fe_2O_3$ spectra of (a) Fe 2p and (b) O 1s. The 0.75g-$C_3N_4@Fe_2O_3$ spectra of (c) Fe 2p, (d) O 1s, (e) C 1s, and (f) N 1s and bulk g-$C_3N_4$ spectra of (g) C 1s and (h) N 1s based on X-ray photoelectron spectroscopy (XPS) analysis–fitting results.

### 3.3 Optical properties

To study the absorbance ranges and band gap energies of the prepared films, the optical absorbance was measured from 300 to 800 nm as shown in Fig. 5(a). Bare $Fe_2O_3$ exhibited a slow absorption edge around 550 nm while the bulk g-$C_3N_4$ showed a steep absorption edge around 430 nm. However, when g-$C_3N_4$

was coated onto $Fe_2O_3$ films in different amounts, notable peaks were observed around 550 nm and the absorption edges became steeper because of g-$C_3N_4$ coating. Thus, all g-$C_3N_4@Fe_2O_3$ films exhibited higher absorption intensities than that of bare $Fe_2O_3$ during the entire UV-visible region, suggesting the enhancement of the absorption ability under
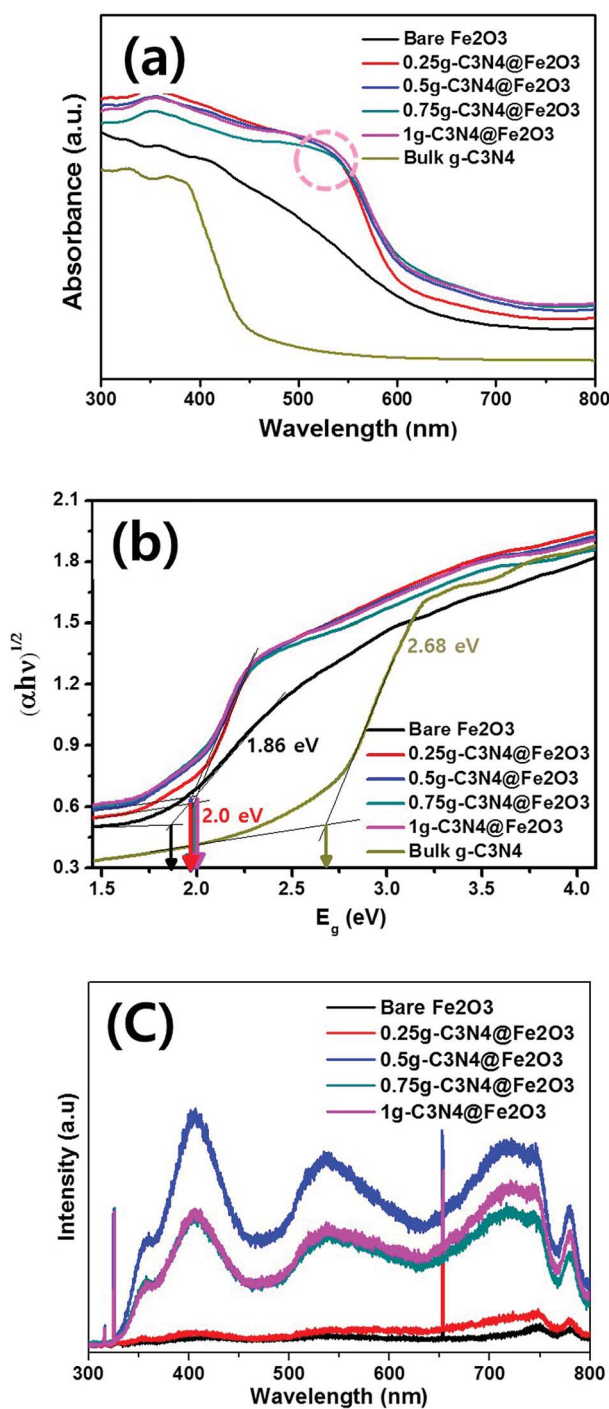
Fig. 5 Band gap energy measurement results based on (a) optical absorbances, (b) calculated absorbances, and (c) photoluminescence for bare $Fe_2O_3$, 0.25g-$C_3N_4$@$Fe_2O_3$, 0.5g-$C_3N_4$@$Fe_2O_3$, 0.75g-$C_3N_4$@$Fe_2O_3$, 1g-$C_3N_4$@$Fe_2O_3$ and bulk g-$C_3N_4$.

illumination. The absorbance was calculated into band gap energies using the Kubelka–Munk function in Fig. 5(b). Although there is a difference in the absorption edge, all g-$C_3N_4$@$Fe_2O_3$ films exhibited similar band gap energies of 2.0 eV. When the g-$C_3N_4$ is coated onto $Fe_2O_3$ nanorod film, the band gap difference has occurred for sure, compared to that of

bare $Fe_2O_3$ film of 1.86 eV. Based on calculated band gap of bulk g-$C_3N_4$, it exhibited 2.68 eV of band gap energy. Therefore, as-prepared heterostructure films provided the higher absorption intensity, with extending its utilization of light irradiation, compared to that of bare $Fe_2O_3$, confirming successful formation of heterostructure film.

Fig. 5(c) shows PL spectra exploring recombination or transfer of photogenerated electrons and hole pairs between $Fe_2O_3$ and g-$C_3N_4$. Typically, large (>70 nm) nanomaterials do not exhibit PL since optical transition is not possible[55] and our $Fe_2O_3$ nanorods also did not show any significant emission peaks. In other words, 0.25g-$C_3N_4$@$Fe_2O_3$ film also showed almost no PL emission peak possibly due to small amounts of g-$C_3N_4$ loading on bare $Fe_2O_3$. The 0.5g-$C_3N_4$@$Fe_2O_3$ showed the highest PL intensity among the samples because of the fast charge recombination. On the other hand, the 1g and 0.75g-$C_3N_4$@$Fe_2O_3$ were observed with similar PL intensity while 0.75g-$C_3N_4$@$Fe_2O_3$ showed lower intensity than that of 1g-$C_3N_4$@$Fe_2O_3$. This means that 0.75g-$C_3N_4$@$Fe_2O_3$ makes good heterojunction of interfaces, reflecting effective separation of electron and hole pairs. Furthermore, the bulk g-$C_3N_4$ was measured for comparison as shown in Fig. S4(d).† As a result, it showed high PL intensity at 423 nm of wavelength, attributing to fast recombination rate of charge carriers in bulky structures. Of all the photoanodes, 0.75g-$C_3N_4$@$Fe_2O_3$ associated with rapid electron movement and thus enhancement of PEC-mediated water splitting and photocatalytic performance.

### 3.4 Photoelectrochemical analysis

We used PEC analysis to evaluate photoresponses in the presence of 0.5 M $Na_2SO_4$ under visible illumination. Fig. 6(a) shows the transient photocurrents during light-chopping. The overall on–off cycles of all films are presented in Fig. S5(a).† During the on–off cycles, when the light was on, the film photoresponses were rapid. In the curves, the strong spikes in the light-on phases reflect electron–hole recombination on the surfaces during photocatalytic reactions. When recombination is slow, the spike peak is broad and the electron–hole combination exhibits a longer lifetime than that of the bare $Fe_2O_3$ film because of effective electron/hole separation during irradiation.[56] Of the various hybrid films, the 0.75g-$C_3N_4$@$Fe_2O_3$ film exhibited slow and broad recombination, associated with a higher photocurrent (1.0 mA) than the other samples. Bare $Fe_2O_3$ exhibited almost no current (ca. 0.005 mA), whereas stepwise g-$C_3N_4$ coating increased the photocurrent proportionately (to 0.25g, 0.5g and 1g $C_3N_4$ values of 0.02, 0.06 and 0.09 mA, respectively). The photocurrent for bulk g-$C_3N_4$ was measured to be 0.04 mA under the same condition, exhibiting similar photocurrent with bare $Fe_2O_3$ and 0.25g-$C_3N_4$@$Fe_2O_3$ film. As expected, the 0.75g-$C_3N_4$@$Fe_2O_3$ film exhibited the highest photocurrent because charge separation was effective; recombination was low after the light came on. Surprisingly, the current was about 200-fold that of the bare $Fe_2O_3$ film because of optimization of the g-$C_3N_4$ coating layer, suggesting that photogenerated electrons and hole pairs separated effectively
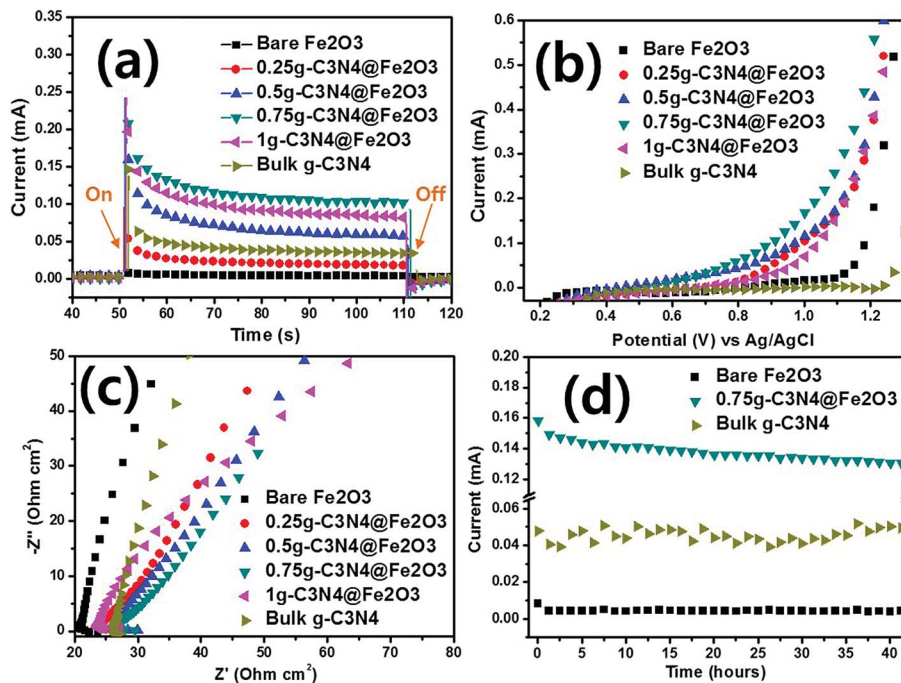
Fig. 6 (a) Photoresponse measurements of transient photocurrents with on/off light. (b) Linear sweep voltammetry (LSV) data. (c) Electrical impedance spectroscopy (EIS) data derived using bare $Fe_2O_3$, 0.25g-$C_3N_4$@$Fe_2O_3$, 0.5g-$C_3N_4$@$Fe_2O_3$, 0.75g-$C_3N_4$@$Fe_2O_3$, 1g-$C_3N_4$@$Fe_2O_3$ and bulk g-$C_3N_4$. (d) The photoresponse stability of bare $Fe_2O_3$ vs. 0.75g-$C_3N_4$@$Fe_2O_3$ vs. and bulk g-$C_3N_4$ under visible irradiation.

due to good formation of interface between g-$C_3N_4$ and $Fe_2O_3$ in heterojunctions.

The photocurrent *versus* applied potential curves of bare $Fe_2O_3$, and the various heterostructures, were assessed using LSV under identical conditions. In the dark, no photoresponse attributable to hybridization was apparent [dashed line in Fig. S5(b)†].[57] In the light [Fig. 6(b)], the bare $Fe_2O_3$ and bulk g-$C_3N_4$ films produced almost no photocurrent according to
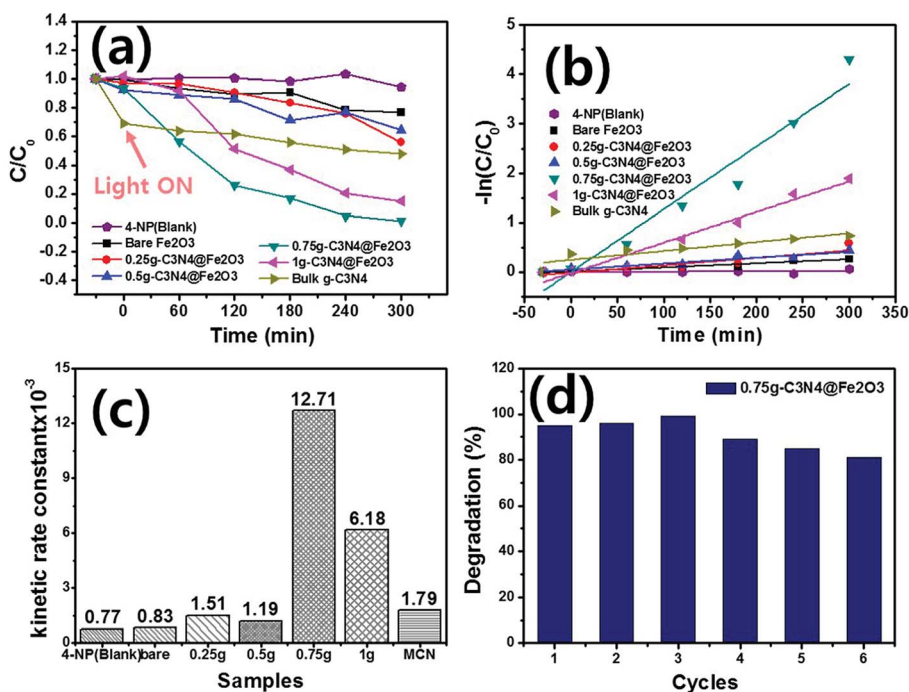


Fig. 7 Photocatalytic degradation of 4-nitrophenol (4-NP). (a) Relative absorbances. (b) Logarithms of absorbances. (c) Kinetic rate constants of 4-NP (blank), bare $Fe_2O_3$, 0.25g-$C_3N_4$@$Fe_2O_3$, 0.5g-$C_3N_4$@$Fe_2O_3$, 0.75g-$C_3N_4$@$Fe_2O_3$, 1g-$C_3N_4$@$Fe_2O_3$ and bulk g-$C_3N_4$. (d) Reusability testing of 0.75g-$C_3N_4$@$Fe_2O_3$ under visible irradiation.

applied potential *versus* Ag/AgCl. In contrast, the various hybrid films exhibited photocurrents. The photoresponses of the 0.25g, 0.5g, and 1g-$C_3N_4$@$Fe_2O_3$ films were similar. The 0.75g-$C_3N_4$@$Fe_2O_3$ film evidenced the highest performance at 1 V *versus* Ag/AgCl. Therefore, the g-$C_3N_4$ coat formed a useful heterojunction with $Fe_2O_3$, reducing the recombination rate of the charge carriers.

EIS was used to measure charge transfers from the g-$C_3N_4$@$Fe_2O_3$/electrolyte interface. In the dark, all films tested (bare $Fe_2O_3$ and the various heterostructures) exhibited higher impedances than in the light [Fig. S5(c)†]. Fig. 6(c) shows the impedances of all samples, where that of bare $Fe_2O_3$ was highest. In the light, the electrons and holes created favor the separation of charge carriers, reducing interface resistance. All g-$C_3N_4$-coated films exhibited smaller arc curves than that of bare $Fe_2O_3$ and bulk g-$C_3N_4$. The $Fe_2O_3$ and g-$C_3N_4$ themselves only, are difficult to overcome the high recombination rate, resulting in high resistance between photocatalysts and electrolyte. Of all films, the 0.75g-$C_3N_4$@$Fe_2O_3$ film exhibited the smallest arc radius, suggesting that the heterostructure can effectively support transfer of the abundant electrons, minimizing surface recombination losses and further improving photocatalytic activities.

After PEC evaluation, we performed stability testing under the conditions shown in Fig. 6(d). Only bare $Fe_2O_3$ and 0.75g-$C_3N_4$@$Fe_2O_3$ were subjected to such testing. The latter film remained photoresponsive to 40 h and bare $Fe_2O_3$ was not photoresponsive. The stability of bulk g-$C_3N_4$ was also conducted for comparison under visible light and it showed unstable photocurrent of 0.04 mA. Despite a slight decrease in the 0.75g-$C_3N_4$@$Fe_2O_3$ photocurrent over time, this remained higher than that of $Fe_2O_3$. Therefore, the 0.75g-$C_3N_4$@$Fe_2O_3$ film was an optimized heterostructure featuring $Fe_2O_3$ and g-$C_3N_4$ coating layers.

## 3.5 Photocatalytic degradation and scavenger test

Photocatalytic degradation of 4-NP by g-$C_3N_4$@$Fe_2O_3$ films under visible light was examined. In order to facilitate photocatalytic reactions, 0.5 mL of $H_2O_2$ was added into 4-NP solution since the 4-NP solution was not degraded at all without presence of $H_2O_2$ during photodegradation evaluation, as shown in Fig. S6.† Fig. 7(a) illustrates the relative absorbance of all samples by the extent of 4-NP degradation over time. The blank was a pure 4-NP solution (thus, assessing spontaneous degradation). Degradation commenced in the dark for 30 min to
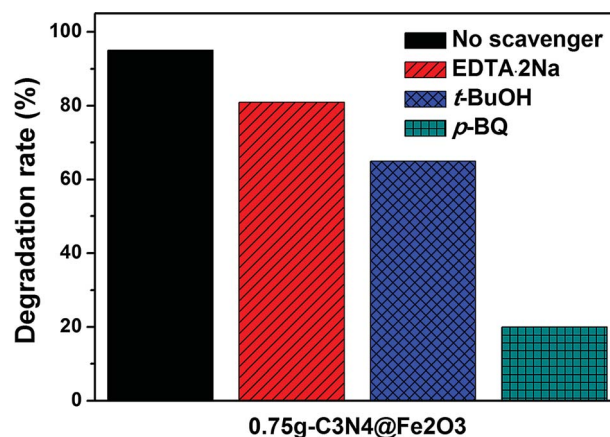


**Fig. 8** The scavenger test of 0.75g-$C_3N_4$@$Fe_2O_3$ without radical trapping, EDTA·2Na, *t*-BuOH and *p*-BQ under visible irradiation.

confirm that adsorption was stable. As a result, few adsorption difference with negligible adsorption properties were observed under a dark state. When the visible light is illuminated, the catalysts started to remove the 4-NP organic pollutant with increasing time. Of the various films, the 0.75g-$C_3N_4$@$Fe_2O_3$ film exhibited the highest extent of degradation, removing all 4-NP by 300 min. The 1g-$C_3N_4$@$Fe_2O_3$ film also afforded rapid degradation because of the extensive g-$C_3N_4$ coating. However, the thick coating inhibited rapid transfer of solar energy into the catalyst; thus, the 0.75g-$C_3N_4$@$Fe_2O_3$ film was more effective than the 1g-$C_3N_4$@$Fe_2O_3$ film. In contrast, the 0.5g and 0.25g-$C_3N_4$@$Fe_2O_3$ films exhibited activities similar to that of bare $Fe_2O_3$ because the g-$C_3N_4$ coatings were thin.[58] Each absorbance graph monitored the 4-NP absorption peak at 325 nm (Fig. S7†). For comparison, the bulk g-$C_3N_4$ was performed for the photocatalytic degradation using 4-NP, exhibiting higher adsorption under the dark condition to be ~31% but showing almost no degradation for 4-NP. To study the kinetic rate, the 4-NP levels were log-transformed and plotted [Fig. 7(b)]. The degradation followed a pseudo first-order equation [the Langmuir–Hinshelwood (L–H) mechanism],[5] mathematically denoted as follows:

$$-\ln(C/C_o) = kt \tag{1}$$

Based on eqn (1), plots of $-\ln(C/C_o)$ *versus* time were linear; $k$ was the kinetic rate constant ($min^{-1}$) of catalytic degradation. The correlation coefficient $R$ is shown in Table 1. The kinetic rate constant for 0.75g-$C_3N_4$@$Fe_2O_3$ ($12.71 \times 10^{-3}$ $min^{-1}$) was ~15-fold higher than that of bare $Fe_2O_3$ ($0.83 \times 10^{-3}$ $min^{-1}$) [Fig. 7(c)]. The $k$ values for 4-NP degradation by 0.25g, 0.5g, 1g-$C_3N_4$@$Fe_2O_3$ and bulk g-$C_3N_4$ were $0.77 \times 10^{-3}$, $1.51 \times 10^{-3}$, $1.19 \times 10^{-3}$, $6.18 \times 10^{-3}$ $min^{-1}$ and $1.79 \times 10^{-3}$ $min^{-1}$, respectively. The reason for enhancement of photocatalytic degradation going from bare $Fe_2O_3$ and bulk g-$C_3N_4$ to g-$C_3N_4$@$Fe_2O_3$ heterostructure films, could be explained by the photoresponse result shown in Fig. 6(d). As shown in the figure, the heterojunction formed between g-$C_3N_4$ and $Fe_2O_3$ coated with g-$C_3N_4$, shows higher current than those of bare $Fe_2O_3$ and

**Table 1** The kinetic constants of photocatalytic degradation

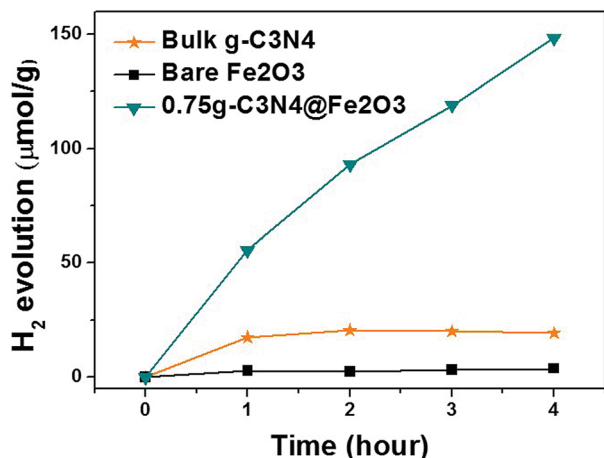| | k $min^{-1}$ | $R^2$ |
|---|---|---|
| 4-Nitrophenol | $0.77 \times 10^{-3}$ | 0.775685 |
| Bare $Fe_2O_3$ | $0.83 \times 10^{-3}$ | 0.90604 |
| 0.25g-$C_3N_4$@$Fe_2O_3$ | $1.51 \times 10^{-3}$ | 0.79317 |
| 0.5g-$C_3N_4$@$Fe_2O_3$ | $1.19 \times 10^{-3}$ | 0.87725 |
| 0.75g-$C_3N_4$@$Fe_2O_3$ | $12.71 \times 10^{-3}$ | 0.9439 |
| 1g-$C_3N_4$@$Fe_2O_3$ | $6.18 \times 10^{-3}$ | 0.95215 |
| Bulk g-$C_3N_4$ | $1.79 \times 10^{-3}$ | 0.78454 |

**Fig. 9** Hydrogen evolution triggered by bulk g-$C_3N_4$ from melamine precursors, by bare $Fe_2O_3$, and by 0.75g-$C_3N_4$@$Fe_2O_3$ using Pt as the co-catalyst under visible irradiation.

bulk g-$C_3N_4$, due to the efficient separation of charge carriers as well as reducing recombination rates at its interface. Consequently, g-$C_3N_4$@$Fe_2O_3$ heterostructure film showed better photodegradation ability with higher kinetic rate constant compared to those of bare $Fe_2O_3$ and bulk g-$C_3N_4$ film. To explore the reusability of 0.75g-$C_3N_4$@$Fe_2O_3$ (which exhibited excellent performance), we recycled the film six times [Fig. 7(d)]. The extent of degradation was >80% after each recycle, indicating good reusability. Furthermore, new 0.75g-$C_3N_4$@$Fe_2O_3$ film was prepared to confirm the repeatability in photodegradation ability under the same condition as shown in Fig. S8.† As a result, it shows similar kinetic rate constant with its error range less than 10%. The 0.75g-$C_3N_4$@$Fe_2O_3$ film exhibited remarkable photocatalytic degradation of 4-NP, attributable to rapid separation of charge carriers at the g-

$C_3N_4$@$Fe_2O_3$ interface and thus promoting photo-oxidation to successfully remove the organic pollutant using a direct z-scheme pathway.

Prior to suggesting possible mechanism of these heterostructures, scavenger tests shown in Fig. 8, are performed to study the photocatalytic reaction in detail. For the photocatalytic activity, there are main free radicals as active species which are hole ($h^+$), hydroxyl radical ($\cdot OH$) and superoxide radical ($\cdot O_2^-$). To observe the radical trapping performances, 0.75g-$C_3N_4$@$Fe_2O_3$ film was used under light illumination. Here, EDTA·2Na was used to capture a $h^+$, *tert*-butanol (*t*-buOH) was used for $\cdot OH$ and *p*-benzoquinone (*p*-BQ) was used for $\cdot O_2^-$. When the photodegradation rate of 0.75g-$C_3N_4$@$Fe_2O_3$ film itself was approximately 95%, EDTA·2Na and *t*-buOH scavengers showed 81% and 65% degradation rates, respectively, suggesting $h^+$ and $\cdot OH$ are not a crucial role in this photocatalytic activity. In contrast, *p*-BQ scavenger exhibited a significant decrease in 4-NP degradation of 20%. Therefore, it was confirmed that $O_2^-$ is found to be the main active species that works for 0.75g-$C_3N_4$@$Fe_2O_3$ film.

### 3.6 Hydrogen evolution and its possible mechanism

We evaluated hydrogen evolution to further explore the photocatalytic activities of the films under visible illumination. Fig. 9 illustrates $H_2$ production by bulk g-$C_3N_4$, bare $Fe_2O_3$, and 0.75g-$C_3N_4$@$Fe_2O_3$ over 4 h. Only the 0.75g-$C_3N_4$@$Fe_2O_3$ film effectively evolved $H_2$; its performance in this context was excellent. Bulk g-$C_3N_4$, made using melamine as precursor and bare $Fe_2O_3$, evolved 4.79 µmol h$^{-1}$ g$^{-1}$ and 0.94 µmol h$^{-1}$ g$^{-1}$ $H_2$, respectively. However, the figure for 0.75g-$C_3N_4$@$Fe_2O_3$ was 37.06 µmol h$^{-1}$ g$^{-1}$, almost 39-fold that of bare $Fe_2O_3$. Generally, $Fe_2O_3$ does not produce $H_2$ because the conduction level of $Fe_2O_3$ is just below the proton reduction potential.[59] Even when Pt is added to bare $Fe_2O_3$ (as a co-catalyst), $H_2$ evolution remains
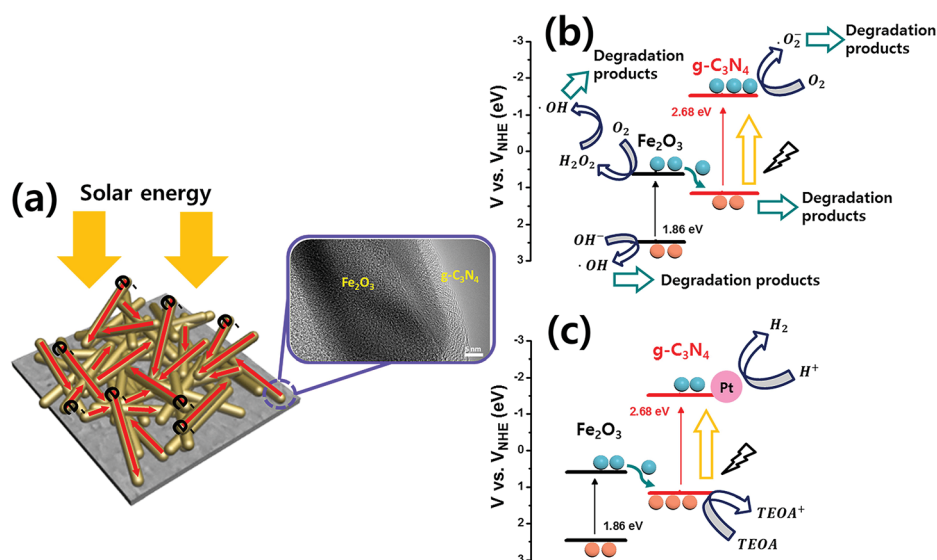


**Fig. 10** The direct z-scheme mechanism of 0.75g-$C_3N_4$@$Fe_2O_3$ heterostructures showing (a) a graphical schematics, bandgap energy diagrams for (b) photocatalytic degradation and (c) $H_2$ evolution.

very low because of rapid recombination of charge carriers. The 0.75g-C$_3$N$_4$@Fe$_2$O$_3$ film forms the optimized interface between Fe$_2$O$_3$ and g-C$_3$N$_4$ for heterojunction, facilitating electron movements due to reducing its recombination rates of charge carriers. Therefore, these results show that the improvement in several properties, like accelerating electron transfer which can subsequently improve the possibility of photoresponse, can be started through 1D structure.[60,61]

Based on these results, the mechanisms of g-C$_3$N$_4$@Fe$_2$O$_3$ heterostructures are shown in Fig. 10. Under solar light irradiation, electrons that are generated are transferred elsewhere by the 1D Fe$_2$O$_3$ nanorods, accompanied by recombination losses attributable to the g-C$_3$N$_4$ coating. The heterostructures can be used to degrade organic pollutants, or to produce gaseous fuels. In order to prove Z-type mechanism from the photocatalytic mechanism, the schematics of band diagram for the heterostructure in Fig. 10, can be used. As shown in Fig. 10, the electrons from the valence band of Fe$_2$O$_3$ is excited to the conduction band of Fe$_2$O$_3$ under the light as they are transferred into the valence band of g-C$_3$N$_4$, for its band edge being very close for the electron movement. Again, the excited electrons in g-C$_3$N$_4$ structure react with oxygen, producing superoxide radical to degrade 4-NP on g-C$_3$N$_4$ surface. To prove this point in terms of band edge between Fe$_2$O$_3$ and g-C$_3$N$_4$, we have measured the valence band of each material using XPS analysis (Fig. S9(a)–(c)†) as well as energy band gap from optical absorbance analysis. As a result, we had measured valence band for g-C$_3$N$_4$ to be 1.13 eV while the conduction band for Fe$_2$O$_3$ was estimated to be 0.62 eV based on the energy band gap measurement (Fig. 5), proving fairly close band edge between Fe$_2$O$_3$ and g-C$_3$N$_4$ with Z-type mechanism. Fig. 10(b) shows the 4-NP degradation mechanism. Under visible light, photogenerated electrons from the Fe$_2$O$_3$ conduction band are transferred to the valence band of g-C$_3$N$_4$, exciting other photogenerated electrons into the g-C$_3$N$_4$ conduction band. The resulting holes in Fe$_2$O$_3$ react with H$_2$O and OH$^-$ to produce ·OH radicals on the surface of Fe$_2$O$_3$. Moreover, the photogenerated electrons in Fe$_2$O$_3$ react with oxygen molecules at the surface of Fe$_2$O$_3$ to produce H$_2$O$_2$. ·OH radicals facilitate the removal of 4-NP organic pollutant. Also, electrons from the g-C$_3$N$_4$ conduction level react with oxygen on the surface of g-C$_3$N$_4$, producing ·O$_2^-$ and allowing 4-NP to be degraded to water.[44] From the scavenger test, the main active species in this reaction system is observed to be ·O$_2^-$ species.[62] When H$_2$ is evolved by heterostructures, the direct z-scheme can be used to explain the mechanism detailed previously[63] [Fig. 10(c)]. When producing H$_2$ using Fe$_2$O$_3$ and g-C$_3$N$_4$, TEOA features hole capture, accelerating electron transfer throughout Pt, and, finally, H$_2$ production. Therefore, the g-C$_3$N$_4$@Fe$_2$O$_3$ heterostructures feature separation of charge carriers at the interface, effectively enriching photocatalytic activities and thus allowing 4-NP degradation and H$_2$ evolution.

## 4. Conclusion

We successfully synthesized 1D g-C$_3$N$_4$@Fe$_2$O$_3$ nanorod/film heterostructures using a solvothermal method, to align the Fe$_2$O$_3$ nanorod film and thermal evaporation to ensure uniform g-C$_3$N$_4$ coating of the film. The thickness of the g-C$_3$N$_4$ coat varied morphologically by the amount of g-C$_3$N$_4$ added compared to bare Fe$_2$O$_3$ All samples exhibited properties on XRD, FT-IR, Raman spectroscopy, and XPS analysis compatible with reliable formation of g-C$_3$N$_4$@Fe$_2$O$_3$ heterostructures. Bare Fe$_2$O$_3$ exhibited poor electron transfer because of rapid recombination of charge carriers. The g-C$_3$N$_4$ coating of Fe$_2$O$_3$ films increased the photoresponse performance, as revealed by transient photocurrent, LSV, and EIS measurements. Furthermore, the 4-NP-degrading photocatalytic activity of g-C$_3$N$_4$ coated Fe$_2$O$_3$ films under visible light was much more rapid than that afforded by bare Fe$_2$O$_3$. Of the various heterostructures, the 0.75g-C$_3$N$_4$@Fe$_2$O$_3$ film exhibited excellent 4-NP degradation for up to 300 min, with a kinetic rate constant of $12.71 \times 10^{-3}$ min$^{-1}$, along with stable recyclability. We also evaluated H$_2$ evolution caused by photocatalytic activity during 4 h of irradiation with visible light. The 0.75g-C$_3$N$_4$@Fe$_2$O$_3$ film produced 37.06 μmol h$^{-1}$ g$^{-1}$ of H$_2$, 39-fold higher than that produced by bare Fe$_2$O$_3$, suggesting that charge separation was efficient and that accumulated electrons accelerated H$_2$ evolution via a direct z-scheme mechanism. Heterostructures composed of g-C$_3$N$_4$ coated onto 1D Fe$_2$O$_3$ nanorods exhibited remarkable photocatalytic activity under visible illumination; electron transfer through 1D structure and charge separation were highly efficient.

## Conflicts of interest

There are no conflicts to declare.

## Acknowledgements

## References

1 J. Ran, M. Jaroniec and S. Z. Qiao, *Adv. Mater.*, 2018, **30**, 1–31.

2 J. Potočnik, *Scinece*, 2007, **315**, 810.

3 J. Gu, J. Yan, Z. Chen, H. Ji, Y. Song, Y. Fan, H. Xu and H. Li, *Dalton Trans.*, 2017, **46**, 11250–11258.

4 A. Boudjemaa, A. Rebahi, B. Terfassa, R. Chebout, T. Mokrani, K. Bachari and N. J. Coville, *Sol. Energy Mater. Sol. Cells*, 2015, **140**, 405–411.

5 X. Liu, L. Zhao, H. Lai, S. Li and Z. Yi, *J. Chem. Technol. Biotechnol.*, 2017, **92**, 2417–2424.

6 Y. H. Li, Y. Wang, L. R. Zheng, H. J. Zhao, H. G. Yang and C. Li, *Appl. Catal., B*, 2017, **209**, 247–252.

7 N. A. Romero and D. A. Nicewicz, *Chem. Rev.*, 2016, **116**, 10075–10166.

8 S. Peiris, J. McMurtrie and H.-Y. Zhu, *Catal. Sci. Technol.*, 2016, **6**, 320–338.

9 H. Hou, F. Gao, L. Wang, M. Shang, Z. Yang, J. Zheng and W. Yang, *J. Mater. Chem. A*, 2016, **4**, 6276–6281.

10 A. Ali and W.-C. Oh, *J. Korean Ceram. Soc.*, 2017, **54**, 308–313.

11 S. Li, X. Shen, J. Liu and L. Zhang, *Environ. Sci.: Nano*, 2017, **4**, 1155–1167.

12 S. Li, S. Hu, W. Jiang, Y. Liu, J. Liu and Z. Wang, *J. Colloid Interface Sci.*, 2017, **501**, 156–163.

13 S. Li, S. Hu, W. Jiang, Y. Liu, Y. Zhou, Y. Liu and L. Mo, *J. Colloid Interface Sci.*, 2018, **521**, 42–49.

14 S. Ye, R. Wang, M.-Z. Wu and Y.-P. Yuan, *Appl. Surf. Sci.*, 2015, **358**, 15–27.

15 A. Kudo and Y. Miseki, *Chem. Soc. Rev.*, 2009, **38**, 253–278.

16 L. Zhang and M. Jaroniec, *Appl. Surf. Sci.*, 2018, **430**, 2–17.

17 J. Zhang, G. Xiao, F.-X. Xiao and B. Liu, *Mater. Chem. Front.*, 2017, **1**, 231–250.

18 S. Li, S. Hu, W. Jiang, Y. Liu, Y. Liu, Y. Zhou, L. Mo and J. Liu, *Beilstein J. Nanotechnol.*, 2018, **9**, 1308–1316.

19 D. M. Arias-Rotondo and J. K. McCusker, *Chem. Soc. Rev.*, 2016, **45**, 5803–5820.

20 J. Low, C. Jiang, B. Cheng, S. Wageh, A. A. Al-Ghamdi and J. Yu, *Small Methods*, 2017, **1**, 1700080.

21 P. Zhou, J. Yu and M. Jaroniec, *Adv. Mater.*, 2014, **26**, 4920–4935.

22 H. Li, W. Tu, Y. Zhou and Z. Zou, *Adv. Sci.*, 2016, **3**, 1500389.

23 H. Katsumata, T. Sakai, T. Suzuki and S. Kaneco, *Ind. Eng. Chem. Res.*, 2014, **53**, 8018–8025.

24 J. C. Wang, L. Zhang, W. X. Fang, J. Ren, Y. Y. Li, H. C. Yao, J. S. Wang and Z. J. Li, *ACS Appl. Mater. Interfaces*, 2015, **7**, 8631–8639.

25 J. Zhang, Y. Hu, X. Jiang, S. Chen, S. Meng and X. Fu, *J. Hazard. Mater.*, 2014, **280**, 713–722.

26 S. Kang, R. C. Pawar, T. J. Park, J. G. Kim, S.-H. Ahn and C. S. Lee, *J. Korean Ceram. Soc.*, 2016, **53**, 393–399.

27 M. Zhang, Y. Duan, H. Jia, F. Wang, L. Wang, Z. Su and C. Wang, *Catal. Sci. Technol.*, 2017, **7**, 452–458.

28 Y. Liao, S. Zhu, J. Ma, Z. Sun, C. Yin, C. Zhu, X. Lou and D. Zhang, *ChemCatChem*, 2014, **6**, 3419–3425.

29 K. S. Lakhi, D. H. Park, K. Al-Bahily, W. Cha, B. Viswanathan, J. H. Choy and A. Vinu, *Chem. Soc. Rev.*, 2017, **46**, 72–101.

30 Y. Wang, J. Sun, J. Li and X. Zhao, *Langmuir*, 2017, **33**, 4694–4701.

31 R. Cheng, L. Zhang, X. Fan, M. Wang, M. Li and J. Shi, *Carbon*, 2016, **101**, 62–70.

32 J. Yu, S. Wang, J. Low and W. Xiao, *Phys. Chem. Chem. Phys.*, 2013, **15**, 16883–16890.

33 B. Lin, C. Xue, X. Yan, G. Yang, G. Yang and B. Yang, *Appl. Surf. Sci.*, 2015, **357**, 346–355.

34 X.-j. Wang, C. Liu, X.-l. Li, F.-t. Li, Y.-p. Li, J. Zhao and R.-h. Liu, *Appl. Surf. Sci.*, 2017, **394**, 340–350.

35 S. Shen, S. A. Lindley, X. Chen and J. Z. Zhang, *Energy Environ. Sci.*, 2016, **9**, 2744–2775.

36 M. Imran, A. B. Yousaf, P. Kasak, A. Zeb and S. J. Zaidi, *J. Catal.*, 2017, **353**, 81–88.

37 J. Wang, J. L. Waters, P. Kung, S. M. Kim, J. T. Kelly, L. E. McNamara, N. I. Hammer, B. C. Pemberton, R. H. Schmehl, A. Gupta and S. Pan, *ACS Appl. Mater. Interfaces*, 2017, **9**, 381–390.

38 J. Wang, C. Qin, H. Wang, M. Chu, A. Zada, X. Zhang, J. Li, F. Raziq, Y. Qu and L. Jing, *Appl. Catal., B*, 2018, **221**, 459–466.

39 X. She, J. Wu, H. Xu, J. Zhong, Y. Wang, Y. Song, K. Nie, Y. Liu, Y. Yang, M.-T. F. Rodrigues, R. Vajtai, J. Lou, D. Du, H. Li and P. M. Ajayan, *Adv. Energy Mater.*, 2017, **7**, 1700025.

40 Y. Xu, S. Huang, M. Xie, Y. Li, H. Xu, L. Huang, Q. Zhang and H. Li, *RSC Adv.*, 2015, **5**, 95727–95735.

41 S. Hu, R. Jin, G. Lu, D. Liu and J. Gui, *RSC Adv.*, 2014, **4**, 24863.

42 H.-M. Xu, H.-C. Wang, Y. Shen, Y.-H. Lin and C.-W. Nan, *J. Appl. Phys.*, 2014, **116**, 174307.

43 L. Wang, X. Lu, C. Han, R. Lu, S. Yang and X. Song, *CrystEngComm*, 2014, **16**, 10618–10623.

44 H. Lin, Y. Liu, J. Deng, S. Xie, X. Zhao, J. Yang, K. Zhang, Z. Han and H. Dai, *J. Photochem. Photobiol., A*, 2017, **336**, 105–114.

45 J.-Y. Lee, M.-C. Tsai, P.-C. Chen, T.-T. Chen, K.-L. Chan, C.-Y. Lee and R.-K. Lee, *J. Phys. Chem. C*, 2015, **119**, 25754–25760.

46 Y. Li, X. Wei, B. Zhu, H. Wang, Y. Tang, T. C. Sum and X. Chen, *Nanoscale*, 2016, **8**, 11284–11290.

47 X. Wang, Y. Liang, W. An, J. Hu, Y. Zhu and W. Cui, *Appl. Catal., B*, 2017, **219**, 53–62.

48 P. V. Zinin, L.-C. Ming, S. K. Sharma, V. N. Khabashesku, X. Liu, S. Hong, S. Endo and T. Acosta, *Chem. Phys. Lett.*, 2009, **472**, 69–73.

49 T. Wang, Y. Li, L. Wang, C. Liu, S. Geng, X. Jia, F. Yang, L. Zhang, L. Liu, B. You, X. Ren and H. Yang, *RSC Adv.*, 2015, **5**, 60114–60120.

50 J. Di, J. Xia, S. Yin, H. Xu, L. Xu, Y. Xu, M. He and H. Li, *J. Mater. Chem. A*, 2014, **2**, 5340.

51 D. Chen, W. Wei, R. Wang, J. Zhu and L. Guo, *New J. Chem.*, 2012, **36**, 1589.

52 J. Wang, B. Feng, J. Su and L. Guo, *ACS Appl. Mater. Interfaces*, 2016, **8**, 23143–23150.

53 L. Liu, J. Wang, C. Wang and G. Wang, *Appl. Surf. Sci.*, 2016, **390**, 303–310.

54 Y. Yan, H. Tang, F. Wu, R. Wang and M. Pan, *Energies*, 2017, **10**, 1–13.

55 N. M. Abdul Rashid, C. Haw, W. Chiu, N. H. Khanis, A. Rohaizad, P. Khiew and S. Abdul Rahman, *CrystEngComm*, 2016, **18**, 4720–4732.

56 D. Li, W. Wang, D. Jiang, Y. Zheng and X. Li, *RSC Adv.*, 2015, **5**, 14374–14381.

57 Y. Liu, F.-Y. Su, Y.-X. Yu and W.-D. Zhang, *Int. J. Hydrogen Energy*, 2016, **41**, 7270–7279.

58 J. Zhang, M. Vasei, Y. Sang, H. Liu and J. P. Claverie, *ACS Appl. Mater. Interfaces*, 2016, **8**, 1903–1912.

59 S. Zhu, F. Yao, C. Yin, Y. Li, W. Peng, J. Ma and D. Zhang, *Microporous Mesoporous Mater.*, 2014, **190**, 10–16.

60 A. Annamalai, P. S. Shinde, A. Subramanian, J. Y. Kim, J. H. Kim, S. H. Choi, J. S. Lee and J. S. Jang, *J. Mater. Chem. A*, 2015, **3**, 5007–5013.

61 L. Jia, J. Xie, C. Guo and C. M. Li, *RSC Adv.*, 2015, **5**, 62611–62618.

62 K. C. Christoforidis, T. Montini, E. Bontempi, S. Zafeiratos, J. J. D. Jaén and P. Fornasiero, *Appl. Catal., B*, 2016, **187**, 171–180.

63 Y.-p. Li, F.-t. Li, X.-j. Wang, J. Zhao, J.-n. Wei, Y.-j. Hao and Y. Liu, *Int. J. Hydrogen Energy*, 2017, **42**, 28327–28336.